A Heuristic for Matrix Product State Simulation of Out-of-Equilibrium Dynamics of Two-Dimensional Quantum Spin Systems

Salvatore Mandrà,* Brayden Ware, Nikita Astrakhantsev, Sergei Isakov, Benjamin Villalonga, Tom Westerhout, and Kostyantyn Kechedzhi

Google Quantum AI, Mountain View, USA

(Received 9 December 2025; accepted 4 August 2026; published 8 September 2026)

Out-of-equilibrium dynamics of non-integrable Hamiltonian many-body quantum systems are characterized by highly entangled wave functions. Near-maximal entanglement arises in systems exhibiting thermalization or pre-thermalization, where the system converges to a steady state with a fixed energy density. Classical simulation of the time dependence of such wave functions requires exponential resources. However, typical computations aim to estimate expectation values of local operators and correlation functions to some expected precision. For thermalizing systems at sufficiently high-energy densities, such computations can be done without storing the full wave function by instead simulating the evolution of the local operator, which requires significantly fewer resources. Nonetheless, constructing such resource-efficient classical algorithms remains a challenge for intermediate energy densities, where simulating both the wave function and operator evolution is costly. In this paper, we propose a heuristic approach to accelerate the convergence of matrix product state (MPS) simulations of expectation values, applicable across a broad range of energy densities. We estimate the desired observables by rescaling the MPS results at low bond dimensions with a factor that depends on the fidelity of the MPS wave function. Using this technique, we simulated the dynamics of the two-dimensional transverse-field Ising model (TFIM) on a 7×8 grid with periodic boundary conditions, using a maximum bond dimension of $\chi = 4096$ on a single A100 GPU, as well as the dynamics of the two-dimensional XY model on grids of size up to 9×9. We compare our TFIM results to similar simulations on a digital quantum processor [R. Haghshenas *et al.* Nature (London) **653**, 56 (2026)], demonstrating excellent agreement and confirming the predictive power of our method.

DOI: 10.1103/qq2m-v44w

I. INTRODUCTION

In recent years, rapid advancements in quantum hardware have revealed a significant separation between the cost of realizing quantum sampling algorithms on quantum processors and (classical) supercomputers [1–6]. These algorithms take advantage of the ability of quantum processors to efficiently prepare and process highly entangled states, whereas classical calculations require storing and processing an exponential number of wave function coefficients to account for entanglement.

This capacity to process highly entangled states also enables the efficient simulation of quantum systems of interest in physics and chemistry in regimes where the classical simulation of the entangled wave function is prohibitively expensive. A number of practical applications of quantum processors rely on quantum simulations of this type, where the task is to estimate the expectation value of a local operator [7]. The least demanding experiment is initialized in an easy-to-prepare state (e.g., a product state) and subsequently evolves subject to the system's Hamiltonian; finally, the expectation value of a local operator is measured.

For a system defined by a local Hamiltonian, estimating expectation values of certain operators classically may require only sub-exponential resources. Indeed, out-of-equilibrium dynamics initialized near the ground state of a gapped Hamiltonian are often characterized by low (area law) entanglement and allow for an efficient matrix product state (MPS) representation. Conversely, initializing far from the ground state generates highly entangled dynamics. However, this is often associated with the phenomenon of thermalization, where expectation values of local observables can be computed by approximating the system's state as locally thermal [8–10]. At sufficiently high-energy densities, the (equilibrium) thermal state is described by a product operator [11] and therefore allows

*Contact author: smandra@google.com

Published by the American Physical Society under the terms of the Creative Commons Attribution 4.0 International license. Further distribution of this work must maintain attribution to the author(s) and the published article's title, journal citation, and DOI.

efficient computation of expectation values. In contrast, out-of-equilibrium dynamics is significantly more complex. Nonetheless, at sufficiently high-energy densities, correlation functions can be described by efficient classical algorithms [12,13], whereas more complex observables present a challenge [14,15]. At intermediate energy densities, constructing efficient classical algorithms even for correlation functions has remained a challenge despite recent progress [16,17].

This intermediate density regime can be studied using quantum processors. Quantum dynamics in the vicinity of a phase transition is of particular interest, as it is characterized by high-energy-density and long-time out-of-equilibrium dynamics. Such out-of-equilibrium dynamics have been studied in a recent experiment [18] on the digital simulation of the transverse field Ising model (TFIM), a prominent benchmark for quantum magnetism and critical phenomena.

In this paper, we introduce a heuristic approach that accelerates the convergence of classical MPS simulations. It allows computing expectation values of local operators using a bond dimension significantly smaller than that needed to represent the state with high precision. More precisely, our heuristic involves rescaling the desired observables by a correction factor that depends only on the total fidelity of the MPS, a parameter readily available during the simulation.

We apply this technique to the dynamics of TFIMs with periodic boundary conditions for grids up to 11×11. In particular, for the 7×8 TFIM, our numerical results agree with the experimental results reported in Ref. [18] within the extrapolated numerical error, confirming the predictive power of our numerical method.

The paper is structured as follows: In Sec. II, we introduce the TFIM and the parameters used in our simulations; in Sec. III, we provide our numerical analysis and results for TFIMs up to 11×11, for which we have exact numerical results for grids up to 6×8; in Sec. IV, we compare the available experimental data for the 7×8 TFIM [18] with our rescaling approach; finally, in Sec. V, we apply our method to the 2D XY model. In Supplemental Material [19], we demonstrate the generalizability of our method to the 3D TFIM.

II. TRANSVERSE-FIELD ISING MODEL

For a general D-dimensional lattice, the TFIM Hamiltonian is given by

$$H = J\sum_{\langle i,j\rangle} Z_i Z_j + h\sum_i X_i = H_{ZZ} + H_X. \tag{1}$$

Here, Z_i and X_i are Pauli operators at site i, the sum $\sum_{\langle i,j\rangle}$ runs over all pairs of nearest-neighbor sites with periodic boundary conditions, J is the coupling strength between neighboring spins, and h represents the strength of the transverse magnetic field.

It is well established that the model exhibits a quantum phase transition at zero temperature, driven by the competition between the interaction term and the transverse field [20–23]. In the case of a ferromagnetic interaction ($J < 0$) and a small transverse field ($h \ll |J|$), the interaction term dominates. This forces adjacent spins to align, causing the system to spontaneously break the global $\mathbb{Z}_2$ symmetry. As the strength of the transverse field h increases, quantum fluctuations are enhanced, tending to disorder the system by aligning the spins in the X-direction. This competition leads to a quantum critical point at a finite value of $|h/J|$, beyond which the long-range ferromagnetic order is destroyed, and the system enters a quantum paramagnetic phase. Away from the ground state in the pre-thermal regime, the TFIM also demonstrates characteristics of a paramagnet-ferromagnet transition at finite temperature.

When simulating the dynamics of the TFIM on digital quantum computers, the continuous time evolution is often approximated using a Suzuki-Trotter decomposition. More precisely, the continuous dynamics of the TFIM is replaced with a second-order Trotter expansion of the form:

$$U(dt) \approx e^{-idtH_X/2} e^{-idtH_{ZZ}} e^{-idtH_X/2}. \tag{2}$$

The unitary $U(dt)$ of a single Trotter step can then be realized by interleaving layers of single-qubit gates with layers of two-qubit gates.

This method discretizes the evolution into a sequence of quantum gates, effectively subjecting the system to a periodic drive. Such periodically driven, or Floquet, many-body systems can exhibit a phenomenon known as Floquet pre-thermalization. Instead of rapidly heating to an infinite-temperature state as might be expected, the system can enter a long-lived, non-trivial steady state that remains close to the initial state (in energy density) for a timescale that is exponentially long in the driving frequency. This pre-thermal phase is characterized by an emergent, nearly conserved effective Hamiltonian, which governs the dynamics of the system before the eventual onset of thermalization. As described in Refs. [24–27], such a pre-thermal phase can survive up to a characteristic Floquet heating time scale on the order of $\tau_H \sim \exp(1/|J|dt)$. Therefore, the thermal physics of the TFIM can be accessed for an exponentially long timescale τ_H.

For our numerical simulations, we initialize the system in a product state of the form:

$$|\Psi(\theta)\rangle = \bigotimes_j (\cos(\theta/2)|0\rangle_j + \sin(\theta/2)|1\rangle_j). \tag{3}$$

On the pre-thermal timescale, the energy is approximately conserved and is equal to its value in the initial state. The latter can be tuned in a broad range by varying $\Delta\theta = \theta - \theta_{\min}$, where $\theta_{\min} = \sin^{-1}[h/(dJ)]$ corresponds to the minimum mean-field energy of the TFIM, H in Eq. (1). Here d is the number of neighbors of a spin on a square lattice $d = 4$. For a sufficiently small $|h/J|$, it is possible to identify the transition between the quantum ferromagnetic and paramagnetic phases by studying the correlation function of the Ising order parameter:

$$\langle Z_{\text{tot}}^2(s)\rangle = \frac{1}{n^2}\sum_{j,k}\langle\Psi(\theta)|(U^\dagger)^s Z_j Z_k (U)^s|\Psi(\theta)\rangle, \qquad (4)$$

where s corresponds to the total number of Trotter steps. Unless otherwise specified, in this paper, we focus on $L_x \times L_y$ grids with $dt = 0.25$, $J = -1$, $h = 2$, and on three "temperatures": a low temperature ($\Delta\theta = 0$), a mid temperature ($\Delta\theta = 2\pi/9$), and a high temperature ($\Delta\theta = 3\pi/9$). The mid temperature is chosen to ensure that the pre-thermal dynamics is close to the phase transition [see Fig. 2b of Ref. [18]]. To simplify the notation, we omit the explicit dependence on s when clear from context.

III. NUMERICAL RESULTS

Our MPS simulations are performed using the time-evolving block-decimation (TEBD) algorithm. This simulation evolves the initial state $|\Psi(\theta_{\min} + \Delta\theta)\rangle$, as defined in Eq. (3), by sequentially applying the gates from the circuit representation of the Trotter steps $(U(dt))^s$ in Eq. (2).

After each gate is applied, the MPS is returned to its canonical form, and a truncation is performed via singular-value decomposition. As in standard TEBD, the MPS is normalized to have unit norm after each truncation, while the truncation fidelity is tracked separately. To ensure that the computational cost of the singular-value decomposition depends only on the bond dimension χ, the orthogonality center is moved to the bond between the MPS sites before performing the decomposition. To further minimize the computational cost, multiple physical qubits are grouped into single MPS sites. More precisely, qubits in each row of an $L_x \times L_y$ grid are split into two groups, and qubits in the same group are then fused together (see Fig. 1). When a two-qubit gate acts on qubits within the same block, the corresponding tensor is updated locally, and the bond dimension remains unchanged. In contrast, when a gate couples qubits in two distinct blocks, it is decomposed as a matrix product operator and applied to the MPS. For gates with a Schmidt rank of 2, such as $e^{-i\phi Z_i Z_j}$, this operation effectively doubles the bond dimension for all virtual bonds located between the two targeted blocks. This blocking technique improves the efficiency of the TEBD algorithm by reducing the number of singular-value decompositions required per time step. Crucially, because of the limited size of the grouped sites, grouping sites together rather than using a one-to-one mapping does not change our numerical results either qualitatively or quantitatively (see Sec. II of Supplemental Material [19] for a discussion on ordering efficiency). For all simulations, unless otherwise specified, the total number of Trotter steps is $s = 20$, and the bond dimensions are powers of 2 ranging from 2 to 4096. We performed all MPS simulations on a single A100 graphics processing unit (GPU) with 80 GB of RAM. To accommodate larger bond dimensions, the MPS sites are stored in CPU RAM and transferred to GPU memory only when required. For the largest bond dimension of $\chi = 4096$ and $s = 20$ Trotter steps, the simulation took roughly 2 days.

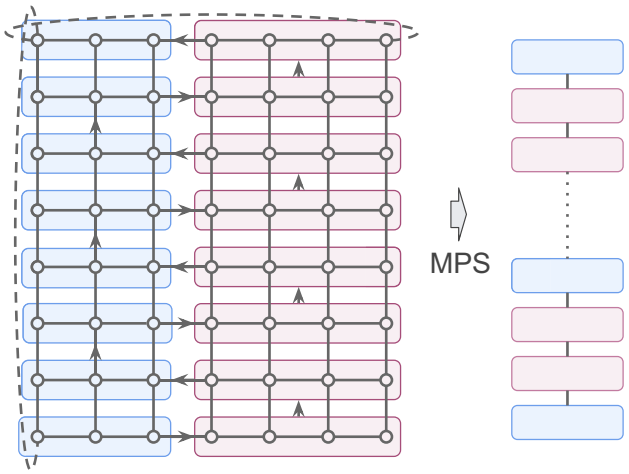


FIG. 1. Left: example of qubit grouping for a $\mathbf{7} \times \mathbf{8}$ grid. Right: final structure of the MPS. Qubits in each row are split into two groups, and qubits in the same group are fused together. The dashed lines correspond to the boundary conditions, while the arrows represent the ordering of the blocks in the MPS.

It is instructive to first consider the expectation value of a single-body observable:

$$\langle Z_{\text{tot}}(s)\rangle = \frac{1}{n}\sum_{j}\langle\Psi(\theta)|(U^\dagger)^s Z_j (U)^s|\Psi(\theta)\rangle. \qquad (5)$$

Estimates of $\langle Z_{\text{tot}}\rangle_{\text{MPS}} = \langle\psi_{\text{MPS}}|Z_{\text{tot}}|\psi_{\text{MPS}}\rangle$ for different bond dimensions, where $|\psi_{\text{MPS}}\rangle$ is the truncated wave function, are shown in Fig. 2. We observe that the estimates at low bond dimensions correlate with the exact results in the following sense. We define the fidelity of the MPS wave function after s time steps as $F_{\text{MPS}}(s) = \prod_{i=1}^{s} f_{\text{MPS}}(i)$. Here, $f_{\text{MPS}}(i)$ denotes the fidelity at step i, calculated as the product of the truncation fidelities following each gate application. For a theoretical analysis of the accuracy of such fidelity estimates, see Ref. [28]. Then, we rescale the estimates for $\langle Z_{\text{tot}}\rangle$ for

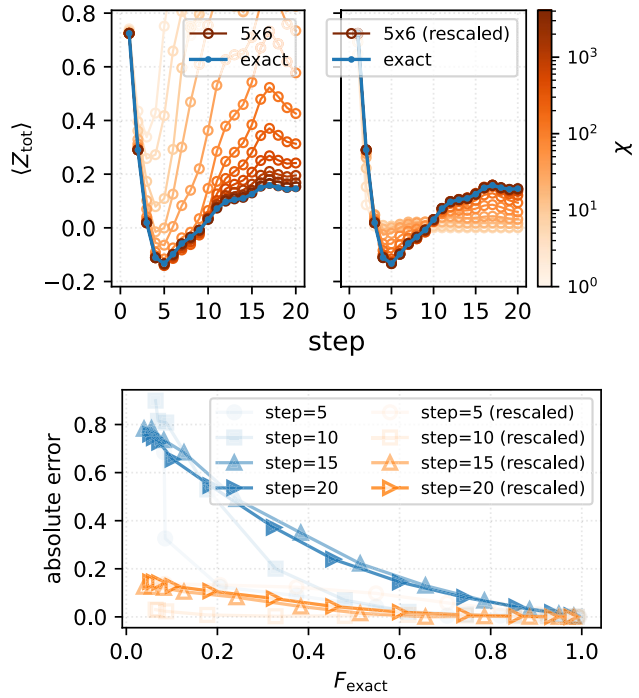


FIG. 2. MPS computation of the magnetization, at fixed $(\Delta\theta, J, h, dt)=(2\pi/9, -1, 2, 0.25)$. The top plots show the convergence of $\langle Z_{\rm tot}\rangle_{\rm MPS}$ without rescaling (left) and with rescaling using the fidelity $F_{\rm MPS}$ (right), see Eq. (6). The bottom plot shows the absolute error at a fixed step as a function of the true fidelity $F_{\rm exact} = |\langle\psi_{\rm exact}|\psi_{\rm MPS}\rangle|^2$, for both $\langle Z_{\rm tot}\rangle_{\rm MPS}$ (filled blue markers) and $\langle Z_{\rm tot}\rangle_{\gamma_{\rm fit}}$ (open orange markers).

different bond dimensions by $F_{\rm MPS}$, i.e., using the relation:

$$\langle\psi|Z_{\rm tot}(s)|\psi\rangle \approx F_{\rm MPS}(s)\langle\psi_{\rm MPS}|Z_{\rm tot}(s)|\psi_{\rm MPS}\rangle. \quad (6)$$

We observe that the estimates for different bond dimensions collapse onto the same curve that approximates the exact result, as shown in Fig. 2. It is worth contrasting our fidelity-based rescaling with standard extrapolation techniques often used in tensor network simulations, such as Richardson extrapolation [29]. Richardson extrapolation typically fits the expectation value of an observable as a function of the discarded weight and extrapolates to the zero-error limit, assuming a smooth functional dependence. However, such an approach fails to accurately capture the dynamics in our case (see also Fig. 3b of Ref. [18] for numerical results obtained via zero-truncation extrapolation in MPS).

This approximation can be understood from the following form of the MPS decomposition of the wave function (after a single time step):

$$U|\psi_{\rm MPS}(i-1)\rangle = \sqrt{f_{\rm MPS}(i)}|\psi_{\rm MPS}(i)\rangle + \sqrt{1-f_{\rm MPS}(i)}|\psi_\perp(i)\rangle, \quad (7)$$

where $|\psi_{\rm MPS}(i)\rangle$ and $|\psi_\perp(i)\rangle$ are, respectively, the MPS wave function at step i and its discarded part after truncation. By construction, $\langle\psi_{\rm MPS}(i)|\psi_\perp(i)\rangle = 0$. Note that for any observable O, the orthogonality of the singular vectors implies that $\langle\psi_\perp(i)|O|\psi_{\rm MPS}(i)\rangle = 0$. This property holds for any single site observable or, more generally, any observable localized within a region where the MPS has been returned to its canonical form. Therefore, the approximation in Eq. (6) amounts to neglecting the contribution from $|\psi_\perp(i)\rangle$ to the final expectation value $\langle Z_{\rm tot}\rangle$, under the assumption that $\langle\psi_\perp|Z_{\rm tot}|\psi_\perp\rangle \approx 0$.

Indeed, $F_{\rm MPS}$ corresponds to the weight of the retained wave function. In our simulations, the expectation value estimate Eq. (6) has a relatively small error even when this weight is small, $F_{\rm MPS} < 1$. In other words, only a small fraction of the norm of the wave function is sufficient to approximate the expectation value. In contrast to the usual estimate $\langle\psi_{\rm MPS}|Z_{\rm tot}(s)|\psi_{\rm MPS}\rangle$, Eq. (6) relies on the properties of the observable. Indeed, replacing $Z_{\rm tot}(s)$ with the identity operator yields a significant error in Eq. (6).

This behavior can be intuitively understood in terms of out-of-equilibrium properties of the two-dimensional TFIM, which demonstrates chaotic characteristics [30,31]. Indeed, the circuit U in Eq. (5) can be characterized by the spectrum of the Floquet Hamiltonian, $U = \sum_E e^{-iE}|E\rangle\langle E|$. Therefore, the expectation value can be expanded in the eigenbasis,

$$\langle O\rangle = \sum_{E,E'}\langle\Psi(\theta)|E\rangle\langle E'|\Psi(\theta)\rangle\langle E|O|E'\rangle e^{-i(E-E')s}. \quad (8)$$

The variance of the energy density in the initial state in Eq. (3), and therefore of the typical energy difference, scales as $1/\sqrt{n}$, which is significant for the system sizes we consider. At sufficiently long times $s \gg 1$, we expect the phases between sufficiently distant energies to be approximately random. Note that, in this limit, we expect the average magnetization to vanish, as expected from the approximately thermal statistics of local observables. The characteristic timescales for such thermalization are short at high energies and much longer at the edge of the spectrum. The latter states typically have low entanglement and are therefore captured by MPS with relatively low bond dimensions, justifying our observation that Eq. (6) holds even when the fidelity is low.

The case of the correlation function $\langle Z_{\rm tot}^2\rangle$ is more complex. Ordered states can contribute an $\mathcal{O}(1)$ value to $\langle Z_{\rm tot}^2\rangle$. Given the large transverse field in our setup ($h = 2$), some of the ordered states are characterized by finite energy density and volume-law entanglement and contribute significantly to $\langle Z_{\rm tot}^2\rangle$. Consequently, the discarded states $|\psi_\perp\rangle$ may have a non-vanishing contribution, $\langle\psi_\perp|Z_{\rm tot}^2|\psi_\perp\rangle \neq 0$. Nonetheless, we observe that low bond dimension estimates rescaled with a fidelity-dependent factor correlate with the exact value. However, there is an

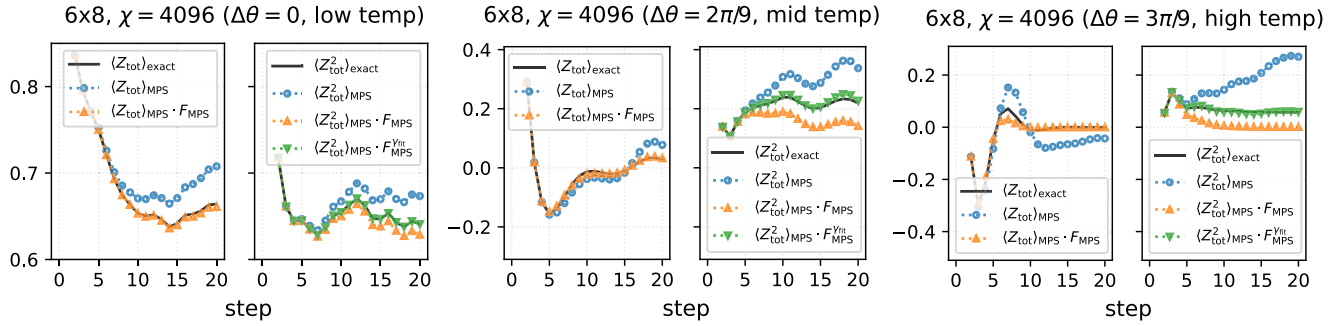


FIG. 3. Comparison of the single-body observable $\langle \mathbf{Z}_{\text{tot}} \rangle$ with $\langle \mathbf{Z}^2_{\text{tot}} \rangle$, at different temperatures. Here, the γ_{fit} values are 0.647, 0.456, and 0.280 for low, mid, and high temperature, respectively.

important difference compared to Eq. (6): the rescaling in this case requires a different factor that is not simply the MPS fidelity F_{MPS}, as shown in Fig. 3,

$$\langle Z^2_{\text{tot}} \rangle_\gamma = \langle Z^2_{\text{tot}} \rangle_{\text{MPS}} \cdot F^{\gamma(n,\chi)}_{\text{MPS}} \tag{9}$$

where the exponent $\gamma(n,\chi)$ is a function depending only on the system size, $n = L_x \times L_y$, and the bond dimension, χ. Note that, in the limit $\chi \to \infty$, the MPS fidelity necessarily converges to unity, $F_{\text{MPS}} \to 1$. Therefore, $\langle Z^2_{\text{tot}} \rangle_\gamma$ is also expected to converge to the exact value $\langle Z^2_{\text{tot}} \rangle_{\text{exact}}$ for a sufficiently large bond dimension.

To determine the scaling parameter $\gamma(n,\chi)$, we performed exact simulations on grids up to 36 qubits. We also performed exact simulations for grids up to 6×8, leveraging the spatial and point-group symmetries induced by the boundary conditions, to serve as a control test. The optimal γ^* is identified by minimizing the maximum absolute error among $s = 20$ Trotter steps between $\langle Z^2_{\text{tot}} \rangle_{\gamma^*}$ and $\langle Z^2_{\text{tot}} \rangle_{\text{exact}}$. As shown in Fig. 4, there is a clear correlation between the optimal γ^* and the rescaled bond dimension. The fitting parameters are reported in Table I. It is important to observe that this correlation is independent of whether a one-to-one mapping or site grouping is used. While the optimal scaling exponent could in principle assume an arbitrary form, the empirical distribution of the unconstrained exponent $\tilde{\gamma} = \log(\langle Z^2_{\text{tot}} \rangle_{\text{ex}} / \langle Z^2_{\text{tot}} \rangle_{\text{MPS}}) / \log F_{\text{MPS}}$, defined as the exponent that reduces the rescaling error to zero for each individual system size and Trotter step, is highly concentrated around the linear ansatz γ^* (see Fig. S2 of Supplemental Material [19]). Figure 5 shows the comparison between $\langle Z^2_{\text{tot}} \rangle_{\text{MPS}}$ and $\langle Z^2_{\text{tot}} \rangle_{\gamma_{\text{fit}}}$ for a 5×6 TFIM with increasing bond dimension. As seen in the figure, $\langle Z^2_{\text{tot}} \rangle_{\gamma_{\text{fit}}}$ converges to $\langle Z^2_{\text{tot}} \rangle_{\text{exact}}$ much faster than the unrescaled $\langle Z^2_{\text{tot}} \rangle_{\text{MPS}}$. To provide a bound on the expected error for larger grids for which we do not have exact results, in Fig. 6 we compare the mean absolute error (left) and maximum absolute error (right) over $s = 20$ steps between $\langle Z^2_{\text{tot}} \rangle_{\text{exact}}$ and $\langle Z^2_{\text{tot}} \rangle_{\gamma_{\text{fit}}}$ (the scaling for other initial temperatures is reported in Fig. S1 of Supplemental Material [19]). More precisely, we observe that the absolute error ϵ correlates strongly with the reduced bond dimension $\log_2 \chi / n$, even for small χ. This allows us to provide an expected error estimate even for grids where exact results are unavailable.

In Fig. 7 we compare the error of our rescaling method against the standard unrescaled estimate and a more complete approximation that explicitly includes the discarded component $|\psi_\perp\rangle$. Our results demonstrate that the off-diagonal terms $\langle \psi_\perp | Z^2_{\text{tot}} | \psi_{\text{MPS}} \rangle$ have a negligible contribution, and that the rescaled estimate is significantly

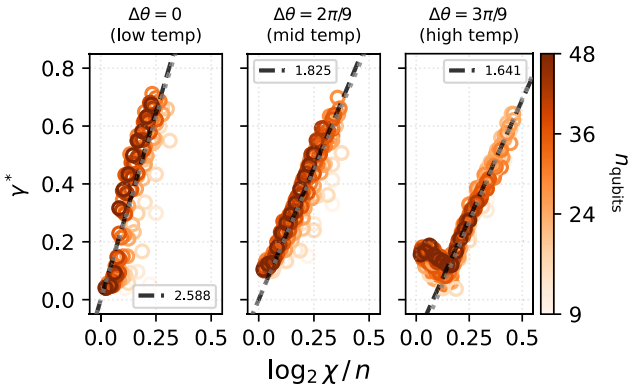


FIG. 4. Fit for the γ^* exponent for three different temperatures. Correlation between the optimal exponent γ^* and the rescaled bond dimension $\log_2 \chi / n$, with varying system size and shape. The gray-dotted lines correspond to the scaling of γ^* if a one-to-one mapping were used instead of grouping sites together. The fit is computed using systems with between 20 and 36 qubits. The fitting parameters are reported in Table I.

TABLE I. Scaling of $\gamma_{\text{fit}} = a \log_2(\chi)/n + b$, by varying the bond dimension χ and system size n. The scalings are reported in Fig. 4.

$\Delta\theta$	a	b
0 (low temperature)	2.588 ± 0.003	0
$2\pi/9$ (mid temperature)	1.8252 ± 0.0003	0
$3\pi/9$ (high temperature)	1.641 ± 0.001	-0.1298 ± 0.0001

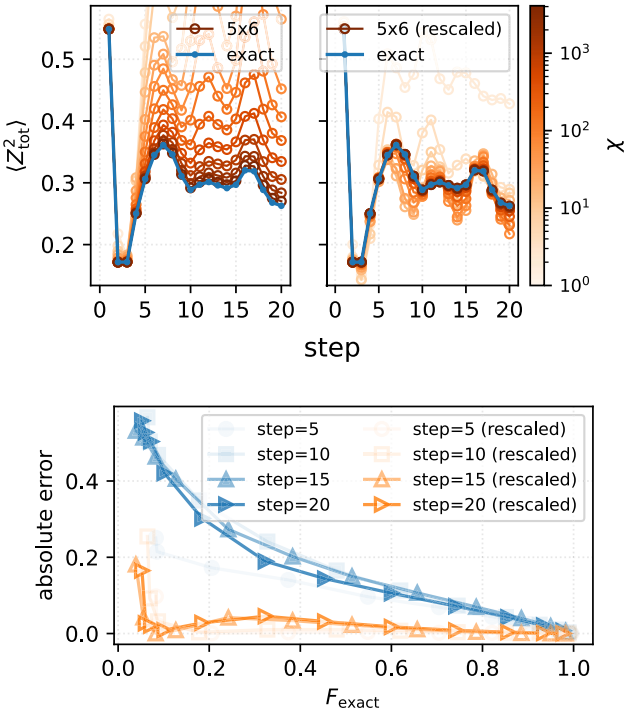


FIG. 5. Comparison of the Ising order parameter with and without rescaling, at fixed $(\Delta\theta, J, h, dt)=(2\pi/9, -1, 2, 0.25)$. The top-left and top-right plots show the convergence of $\langle Z^2_{\rm tot}\rangle_{\rm MPS}$ and $\langle Z^2_{\rm tot}\rangle_{\gamma_{\rm fit}}$, respectively, with increasing bond dimension. The bottom plot shows the absolute error at a fixed step as a function of the true fidelity $F_{\rm exact} = |\langle\psi_{\rm exact}|\psi_{\rm MPS}\rangle|^2$, for both $\langle Z^2_{\rm tot}\rangle_{\rm MPS}$ (filled blue markers) and $\langle Z^2_{\rm tot}\rangle_{\gamma_{\rm fit}}$ (open orange markers).

more accurate than the unrescaled one and performs comparably to the approximation that includes $|\psi_\perp\rangle$. Note that the vanishing of the off-diagonal terms is consistent with the qualitative picture of gradual randomization of phases in Eq. (8) that we introduced above. Equation (9) suggests that additional MPS truncation error compared to Eq. (6) has an effect of an overall damping factor. This invites an analogy with a white noise error model in random circuits [1], where errors translate into a

TABLE II. Fitting parameters for the expected error $\epsilon = K\chi^{\alpha/n}$, by varying the initial parameter $\Delta\theta$. $(K,\alpha)_{\rm mean}$ and $(K,\alpha)_{\rm max}$ correspond to the fitting parameters for the expected mean absolute error and the expected maximum absolute error, respectively.

$\Delta\theta$	$(K,\alpha)_{\rm mean}$	$(K,\alpha)_{\rm max}$
0 (low temperature)	$(0.18\pm0.02,$ $-25.5\pm0.7)$	$(0.40\pm0.04,$ $-24.8\pm0.6)$
$2\pi/9$ (mid temperature)	$(0.24\pm0.02,$ $-24.4\pm0.6)$	$(0.59\pm0.06,$ $-22.6\pm0.6)$
$3\pi/9$ (high temperature)	$(0.46\pm0.05,$ $-24.2\pm0.7)$	$(1.3\pm0.2,$ $-24.0\pm0.8)$

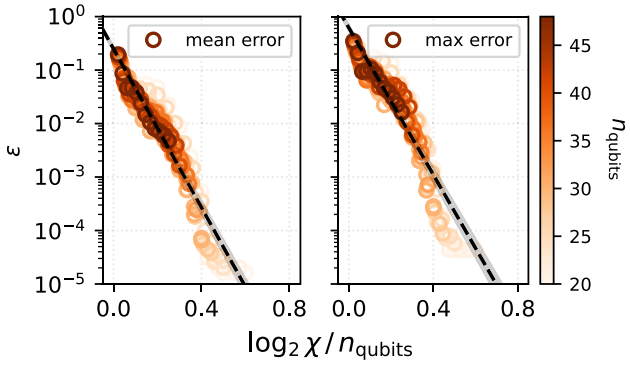


FIG. 6. Scaling of the absolute error between the rescaled $\langle Z^2_{\rm tot}\rangle_{\gamma_{\rm fit}}$ and the exact $\langle Z^2_{\rm tot}\rangle_{\rm exact}$, at fixed $(\Delta\theta, J, h, dt)=(2\pi/9, -1, 2, 0.25)$. The plot shows the mean absolute error (left) and the maximum absolute error (right) between $\langle Z^2_{\rm tot}\rangle_{\gamma_{\rm fit}}$ and $\langle Z^2_{\rm tot}\rangle_{\rm exact}$ over $s = 20$ steps for different grid sizes and bond dimensions χ. The regression $\epsilon = K\chi^{\alpha/n}$ is computed by considering only instances with at least 20 qubits (see Table II for the fitting parameters). The shaded area corresponds to the linear regression error. See also Fig. S1 in Supplemental Material [19].

damping factor upon random twirling of the state of the system. Within the scope of this paper, Eq. (9) is an empirical observation. We leave further theoretical justification of this property for future study.

In Fig. 8, we compare our rescaling technique against the exact results for the 6×8 TFIM across the three different effective temperatures. For each case, we identified the optimal $\gamma_{\rm fit}$ and the corresponding extrapolated error, following the procedures detailed for the mid-temperature case, as shown in Figs. 4 and 6. The

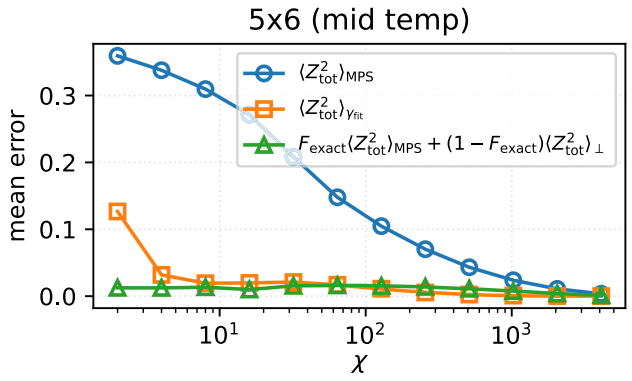


FIG. 7. Mean absolute error of the Ising order parameter as a function of the bond dimension χ. The plot shows the absolute error, averaged over 20 Trotter steps, for the Ising order parameter: without rescaling ($\langle Z^2_{\rm tot}\rangle_{\rm MPS}$), with rescaling via the fidelity ($\langle Z^2_{\rm tot}\rangle_{\gamma_{\rm fit}}$), and with the inclusion of the discarded component after truncation ($F_{\rm exact}\langle Z^2_{\rm tot}\rangle_{\rm MPS} + (1-F_{\rm exact})\langle Z^2_{\rm tot}\rangle_\perp$). Here, $F_{\rm exact} = |\langle\psi_{\rm exact}|\psi_{\rm MPS}\rangle|^2$. To evaluate $|\psi_\perp\rangle$, we concurrently evolved the MPS and exact simulations, performing a Gram-Schmidt orthogonalization at the end of each Trotter step to extract $|\psi_\perp\rangle$ from $|\psi_{\rm exact}\rangle$.

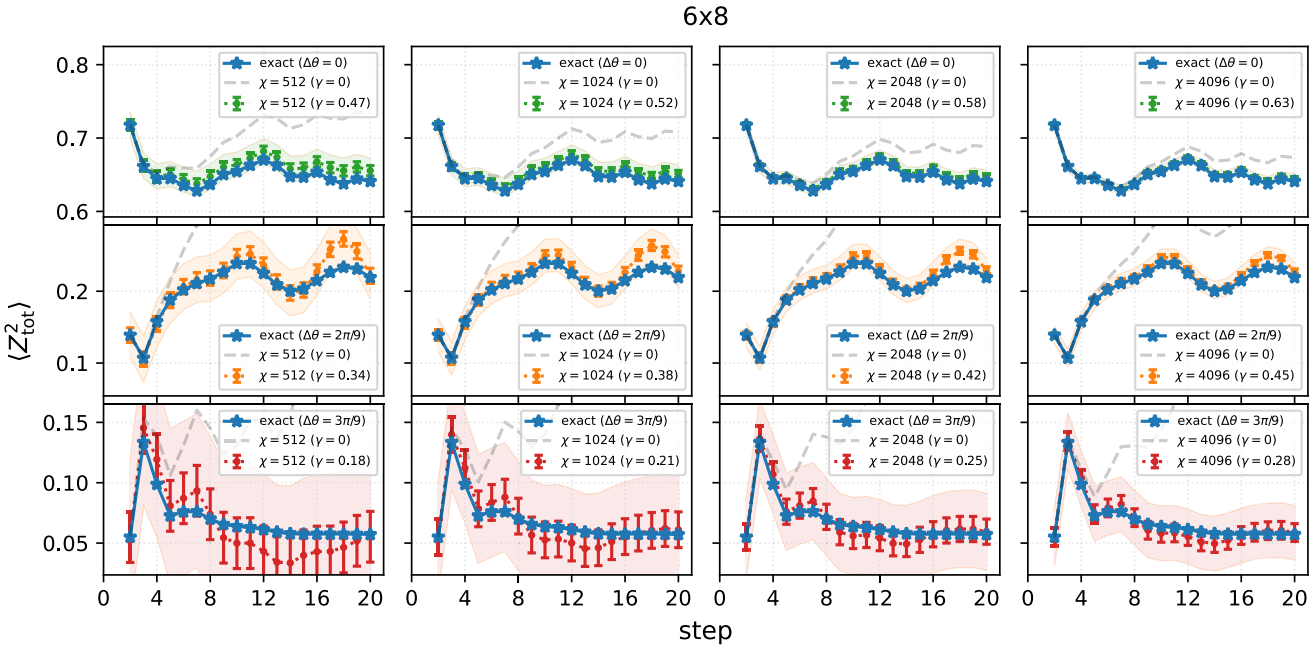


FIG. 8. Numerical simulations of a $\mathbf{6 \times 8}$ TFIM for three different initial temperatures by varying the maximum bond dimension χ. For each temperature, we identified the optimal γ_{fit} and the corresponding extrapolated error, following the procedures detailed for the mid-temperature case, as shown in Figs. 4 and 6. The blue-starred lines represent the exact results. The orange-circled lines correspond to our numerical results for $\langle Z^2_{\text{tot}} \rangle_{\gamma_{\text{fit}}}$, with the error bars (shaded areas) corresponding to the estimates from the mean (maximum) absolute error from Fig. 6. For comparison, the gray-dashed lines correspond to the value of $\langle Z^2_{\text{tot}} \rangle_{\text{MPS}}$ without any rescaling. For all temperatures, $\langle Z^2_{\text{tot}} \rangle_{\gamma_{\text{fit}}}$ is within the maximum error bound of $\langle Z^2_{\text{tot}} \rangle_{\text{exact}}$.

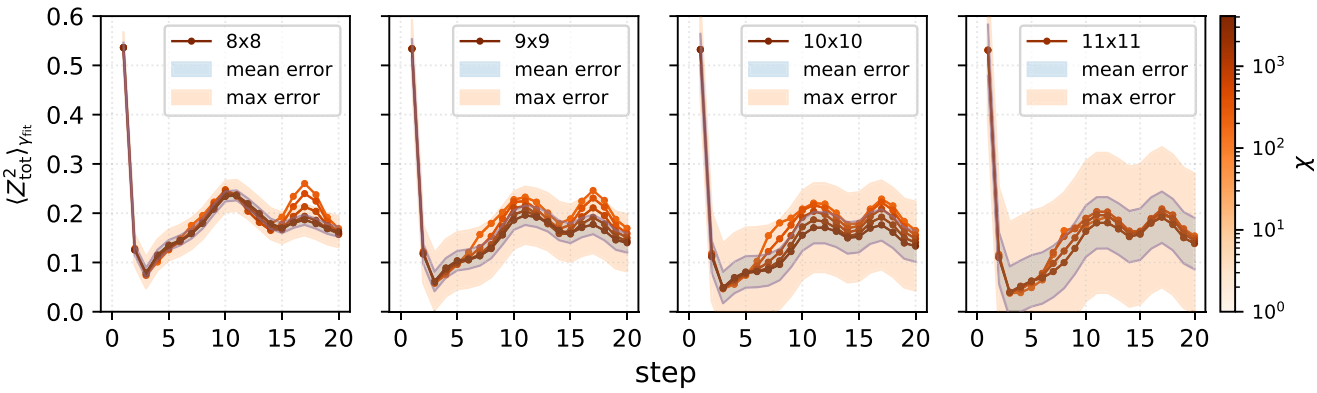


FIG. 9. Numerical results for $\langle \boldsymbol{Z^2_{\text{tot}}} \rangle_{\boldsymbol{\gamma_{\text{fit}}}}$ for larger grids, at fixed $\boldsymbol{\Delta\theta = 2\pi/9}$ (mid temperature). The plots show the rescaled $\langle Z^2_{\text{tot}} \rangle_{\gamma_{\text{fit}}}$ for different grid sizes, with varying maximum bond dimensions (only bond dimensions with $\chi \geq 256$ are visualized). The largest bond dimension for all grids except 11×11 is $\chi = 4096$. For the 11×11 grid, the maximum bond dimension is $\chi = 2048$. The shaded areas correspond to the extrapolated mean absolute error and the extrapolated maximum absolute error for the largest available bond dimension, obtained from Fig. 6.

blue-starred lines represent the exact results, while the orange-circled lines show our numerical results for $\langle Z^2_{\text{tot}} \rangle_{\gamma_{\text{fit}}}$. The error bars (shaded areas) correspond to the estimated mean (maximum) absolute errors. In all instances, our rescaling approach successfully predicts the exact value of $\langle Z^2_{\text{tot}} \rangle$ within the estimated maximum error bound.

We have also extended our simulations to larger TFIM grids up to 11×11, with a maximum bond dimension of $\chi = 4096$ (and $\chi = 2048$ for the 11×11 grid). Due to memory limitations, we used a one-to-one mapping for these simulations instead of grouping sites. The results are summarized in Fig. 9, which shows the convergence of $\langle Z^2_{\text{tot}} \rangle_{\gamma_{\text{fit}}}$ with increasing bond dimension χ for different

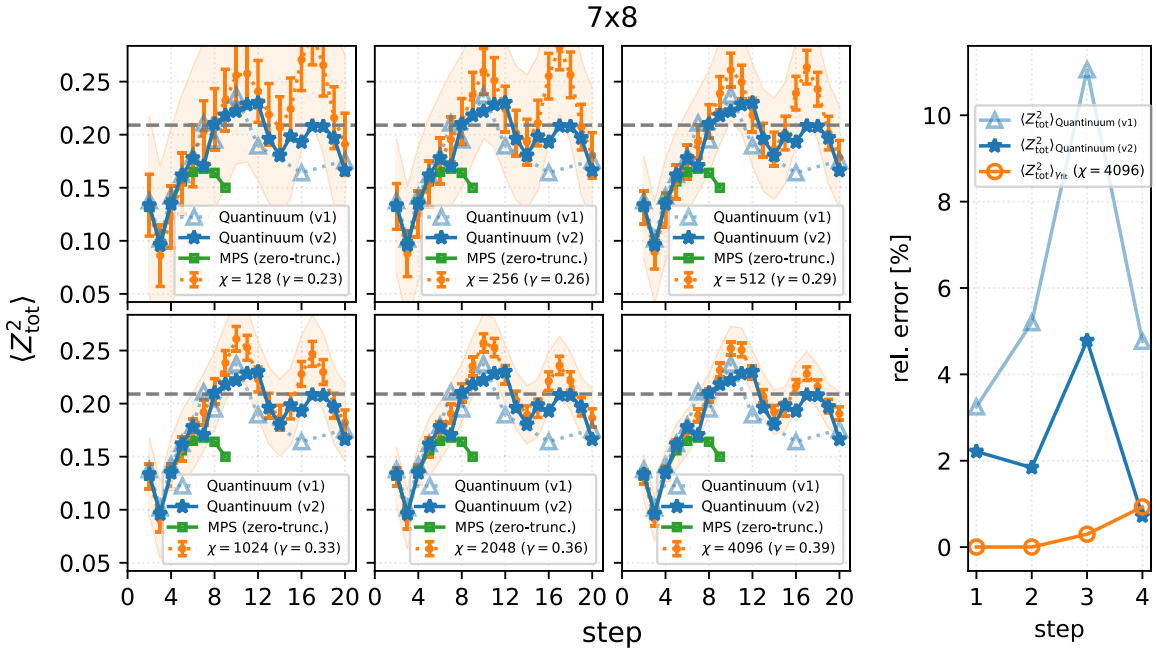


FIG. 10. Left: numerical simulations of a $\mathbf{7 \times 8}$ TFIM by varying the maximum bond dimension χ. Right: comparison against exact results. The blue-starred and blue-triangled lines represent the results from the Quantinuum H2 device before [32] and after [18] the implementation of their improved error correction protocol. We also report the zero-truncation MPS results from Ref. [18]. The orange-circled lines correspond to our numerical results for $\langle Z^2_{\text{tot}} \rangle_{\gamma_{\text{fit}}}$, with the error bars (shaded areas) corresponding to the estimates of the mean (maximum) absolute error from Fig. 6. The dashed horizontal line corresponds to the expected thermal value of $\langle Z^2_{\text{tot}} \rangle$ using an MPS purification ansatz (from Ref. [18]).

grid sizes. The purple-shaded area and the orange-shaded areas correspond, respectively, to the mean absolute error and the maximum absolute error extrapolated from Fig. 6 for the largest available bond dimension for the given grid size. Unfortunately, without verification against exact or error-bounded simulations, we are unable to guarantee that the results we observe in Fig. 9 are converging to the correct $\langle Z^2_{\text{tot}} \rangle$ for the largest systems. A better understanding of the functional form of the factor and a more rigorous analysis of the error of this approximation may allow computing $\langle Z^2_{\text{tot}} \rangle$ without relying on any extrapolation. We leave this for future study.

IV. COMPARISON TO EXPERIMENTAL RESULTS ON 7×8 GRIDS

In a recent paper [18], the TFIM was simulated on a 56-qubit trapped-ion quantum processor, the Quantinuum H2. This gate-based machine is universal, allowing for the flexible implementation of quantum simulations. The native two-qubit gate implemented on the hardware is the $U_{ZZ}(\phi) = \exp(-i\phi Z \otimes Z/2)$ gate, which is used directly to construct the Trotter steps for the simulation without further decomposition.

Using a combination of different error mitigation protocols, the authors of Ref. [18] simulated the quantum dynamics of the 7×8 TFIM up to $s = 20$ Trotter steps (see Fig. 3b in Ref. [18]). To benchmark their quantum simulations, the authors employed a comprehensive suite of state-of-the-art classical numerical methods, including projected entangled pair state simulations with various compression schemes such as belief propagation. However, these classical methods fail after just a few Trotter steps [18].

In contrast, we demonstrate that the correlation function of the Ising order parameter $\langle Z^2_{\text{tot}} \rangle$ can be classically simulated for the 7×8 TFIM using a bond dimension of $\chi = 4096$. Figure 10 (left) shows our numerical simulations for the 7×8 TFIM with varying maximum bond dimensions. The blue-starred and blue-triangled lines represent the results from the Quantinuum H2 device before [32] and after [18] the improved error mitigation protocol, respectively. The orange-circled lines correspond to our numerical results for $\langle Z^2_{\text{tot}} \rangle_{\gamma_{\text{fit}}}$, with the error bars (shaded areas) corresponding to the estimates from the mean (maximum) absolute error from Fig. 6. More precisely, our numerical results are in excellent agreement with the new experimental results from the Quantinuum H2 device, which are now within our estimated error bounds. The accuracy of our numerical results is further corroborated by the fact that our MPS prediction $\langle Z^2_{\text{tot}} \rangle_{\gamma_{\text{fit}}}$ oscillates around the expected thermal value for the Floquet Hamiltonian (to $\mathcal{O}(dt^2)$), computed in the canonical ensemble via an MPS purification ansatz [18], as

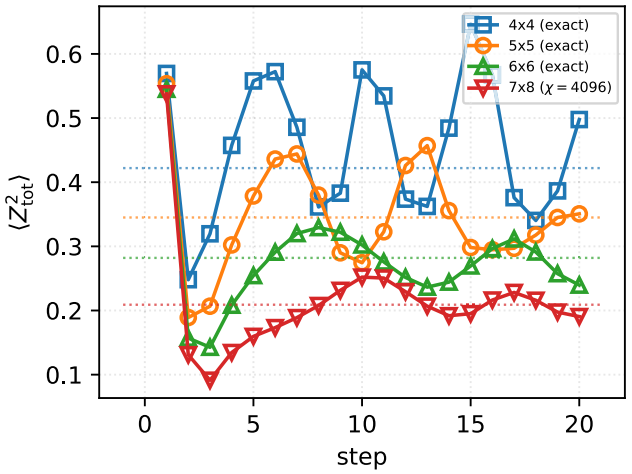


FIG. 11. Expected thermal value of $\langle \boldsymbol{Z}^2_{\mathrm{tot}} \rangle$ for the Floquet Hamiltonian computed in the canonical ensemble using an MPS purification ansatz (from Ref. [18]), compared to either $\langle \boldsymbol{Z}^2_{\mathrm{tot}} \rangle_{\mathrm{exact}}$ or $\langle \boldsymbol{Z}^2_{\mathrm{tot}} \rangle_{\gamma_{\mathrm{fit}}}$. Our numerical $\langle Z^2_{\mathrm{tot}} \rangle_{\gamma_{\mathrm{fit}}}$ for the 7×8 system oscillates around the expected thermal value, corroborating its validity. Results for the expected thermal values are from Ref. [18].

shown in Fig. 11. Finally, Fig. 10 (right) shows the comparison of both the MPS prediction and experimental results against exact results obtained using exact tensor network contraction, up to $s = 4$.

V. XY MODEL

To evaluate the generalizability of the rescaling heuristic beyond the TFIM, we apply it to the quench dynamics of the two-dimensional XY model. This choice introduces several physical ingredients absent from the TFIM dynamics considered in the previous sections: a conserved U(1) charge in the system and the presence of vortex excitations in addition to spin flip (magnon) excitations which change the type of order in the system.

The XY Hamiltonian is given by

$$H_{XY} = \frac{g}{2} \sum_{\langle i,j \rangle} (X_i X_j + Y_i Y_j). \tag{10}$$

Here, X_i and Y_i are Pauli operators at site i, the sum runs over all pairs of nearest-neighbor sites, and g is the coupling strength between neighboring spins. In this section, we consider open boundary conditions on two-dimensional rectangular grids of size $L_x \times L_y$, with $n = L_x L_y$ total sites.

The XY model exhibits a finite-temperature phase transition of the Berezenskii-Kosterlitz-Thouless type [33–35]. The equilibrium properties of this model, including the properties of its critical point, have been characterized with quantum Monte Carlo simulations [36–40]. The order parameter sensitive to the phase transition is the staggered, in-plane magnetization

$$\vec{X}_{\mathrm{tot}} = \frac{1}{n} \sum_j (-1)^j \vec{X}_j, \tag{11}$$

where $\vec{X}_j$ denotes the two-component vector $\{X_j, Y_j\}$, and $(-1)^j$ represents a staggered pattern of ± 1 for lattice sites j. For an equilibrium thermal state $\exp(-\beta H_{\mathrm{XY}})$, the phase transition is detectable via correlations of the order parameter components, which take the following form:

$$\langle (-1)^r X_i X_{i+r} \rangle \sim r^{-\lambda} e^{-r/\xi}, \tag{12}$$

where ξ diverges at and below the critical temperature T_{BKT} [37]. The dynamics of the order parameter, both equilibrium and the non-equilibrium quench studied here, have not been thoroughly explored, partly due to the challenge of classically simulating two-dimensional quantum dynamics at finite energy density.

A. State preparation and dynamics

We aim to prepare initial states with definite values of the conserved U(1) charge across a range of distinct energy densities. Product states are insufficient for this purpose: product states where each spin aligns with the Z-axis have definite values of $\langle Z_{\mathrm{tot}} \rangle$, but $\langle H_{\mathrm{XY}} \rangle = 0$ for all such states. Conversely, product states of spins rotated away from the Z-axis do not have definite values of $\langle Z_{\mathrm{tot}} \rangle$. Instead, we use the following family of initial states to begin our quench dynamics:

$$|\psi_0(\tau)\rangle = \exp\left(-i \frac{\pi}{8} H_Z\right) \exp(-i\tau H_{\mathrm{XY}}) |\mathrm{Neel}\rangle, \tag{13}$$

where $H_Z = \sum_j (-1)^j Z_j$, and $|\mathrm{Neel}\rangle$ is the ground state of H_Z. These states are notable because they access a relatively wide range of energies with small values of τ [see Fig. S3(a) of Supplemental Material [19]]. Since τ is small, $|\psi_0(\tau)\rangle$ can be prepared with a shallow digital quantum circuit after Trotterization of the H_{XY} evolution as described in Sec. V. More importantly for this work, these initial states can be easily prepared as MPS without incurring significant truncation errors for the system sizes considered. Specifically, we focus on three states with values $g\tau = 0.02\pi$, $g\tau = 0.06\pi$, and $g\tau = 0.10\pi$, which cover a broad range of initial energy densities [see Fig. S3(a) of Supplemental Material [19]]. We use a time step of size $g\delta\tau = 0.02\pi$ for the numerical simulations of this state preparation, which correspond to 1, 3, and 5 Trotter steps, respectively. The evolution for this state preparation is sufficiently short—and the generated entanglement sufficiently small—that these states are captured with high accuracy using MPS of modest bond dimensions. As reported in Fig. S3(b) of Supplemental Material [19], the necessary bond dimension scales exponentially

with the width L_y of the rectangular grid, the expected scaling for states with only short-range entanglement.

Unlike the Ising model simulations, the states we consider are all in the high-temperature phase of the XY model. The energy density of the BKT transition is known from Ref. [38], which reports a value of $\epsilon_c \approx -0.53g$ for the energy density per bond near the transition temperature. This value is not reached by the family of states in Eq. (13). Incidentally, this energy density is quite close to the ground-state energy density $\epsilon_g \approx -0.55g$. Consequently, for the sizes n considered in this paper, states with energy density less than ϵ_c have very few excitations above the ground state.

The signal we consider is the dynamics of the total correlation function

$$\langle X_{\mathrm{tot}}^2\rangle(t) = \frac{1}{n^2}\sum_{j,k}(-1)^{j-k}\langle X_j X_k\rangle(t), \tag{14}$$

which can be expressed as a second moment of a component of the order parameter [Eq. (11)]. As we are in the high-temperature phase, we expect via Eq. (12) that in equilibrium this quantity decays like $1/n$ for large n.

For the purposes of our dynamics simulations, we approximate the continuous time evolution of the XY Hamiltonian with a Suzuki-Trotter decomposition. We use the depth 7, second-order decomposition based on splitting the Hamiltonian into four sets of terms that each act only on non-overlapping sets of bonds.

$$U(\delta t) \approx e^{-i\delta t H_A/2}e^{-i\delta t H_B/2}e^{-i\delta t H_C/2}e^{-i\delta t H_D}\cdot e^{-i\delta t H_C/2}e^{-i\delta t H_B/2}e^{-i\delta t H_A/2}. \tag{15}$$

Specifically, this splitting divides the bonds into horizontal bonds starting on even (H_A) or odd (H_B) columns and vertical bonds starting on even (H_C) or odd (H_D) rows. The Trotter step size δt is chosen to ensure that the contributions of the Trotter error are negligible for the purposes of our MPS error analysis; we find that setting $g\delta t = 0.05\pi$ is sufficient for this purpose. Our quench dynamics analysis focuses on the time range $0 \le gt \le 2\pi$, for which the total number of Trotter steps is 40.

B. Numerical results

As described in Sec. III, our numerical simulations are performed with the TEBD algorithm [41]. The simulation first constructs the initial state Eq. (13) as an MPS subsequently evolves it by sequentially applying $U(\delta t)$ defined in Eq. (15). In contrast to the TFIM simulations, for the XY model we use a one-to-one mapping of qubits to MPS sites and do not block multiple physical qubits into single MPS sites.

Our exact simulations of the XY model cover rectangular grids of sizes 4×4, 5×4, 5×5, 6×5, and 6×6; MPS simulations are done for these grids with bond dimensions up to 4096. Throughout, we use fits derived by comparing MPS to exact data only on grids up to 6×5 qubits, reserving the exact 6×6 data for validating the derived fits. Additionally, we show results from MPS simulations on grids of size 7×6, 7×7, 8×8, and 9×9 to demonstrate how our extrapolations yield predictions for dynamics beyond the reach of exact simulation. As for the TFIM, the total truncated weight in our MPS simulations is tracked through the MPS fidelity F_{MPS} [see Fig. S3(c) of Supplemental Material [19]].

Our analysis of the order parameter dynamics proceeds analogously to the TFIM case. For each initial state, bond dimension χ, and system size n, we determine the optimal γ^* that minimizes the distance between the exact signal $\langle X_{\mathrm{tot}}^2\rangle_{\mathrm{exact}}$ and the rescaled MPS signal $\langle X_{\mathrm{tot}}^2\rangle_{\mathrm{MPS}}F_{\mathrm{MPS}}^{\gamma}$ across the considered time range (reported in Fig. S4 of Supplemental Material [19]). As for the TFIM, we observe a correlation between γ^* and the rescaled bond dimension $\log_2\chi/n$, albeit with some significant deviations. We will see below that despite these deviations, rescaling by $F_{\mathrm{MPS}}^{\gamma}$ using a simple linear model for γ still greatly accelerates convergence on system sizes both within and beyond the reach of our training dataset, compared to numerics that are unscaled or scaled with F_{MPS}. We introduce two deviations from the fitting procedure used for the TFIM. First, we find that bond dimensions that are too small to accurately represent the initial state $|\psi_0(\tau)\rangle$ show distinct trends in γ^* and poor-quality dynamics $\langle X_{\mathrm{tot}}^2\rangle_{\mathrm{MPS}}(t)$. Thus, we exclude these bond dimensions from our fits and subsequent plots; specifically, we use the cutoff $F_{\mathrm{MPS}}(t=0) > 0.99$ [see Fig. S3(b) of Supplemental Material [19]]. Second, we observe that for small sizes and very large bond dimensions, where the fidelity remains close to 1 across all times, $\langle X_{\mathrm{tot}}^2\rangle_{\mathrm{MPS}}F_{\mathrm{MPS}}^{\gamma}$ is highly insensitive to the choice of γ. In these cases, the resulting γ^* does not exhibit any discernible trend. We use a cutoff $F_{\mathrm{MPS}}(t_f) < 0.95$ to ensure sensitivity as γ is varied, where t_f is the final time included in the fit.

To see how rescaling by $F_{\mathrm{MPS}}^{\gamma}$ performs, we first plot a comparison of rescaled MPS and corresponding exact data for 6×6 systems with a bond dimension of 4096 in Fig. 12. The 6×6 exact data were not used to predict the exponent γ used here; instead, the rescaling exponent is drawn from the fits reported in Fig. S4 of Supplemental Material [19], which use data up to 30 qubits only. We find that the accuracy of the rescaled data is quite high for early times but begins to deviate gradually as time progresses. We show 40 Trotter steps here, each of size $g\delta t = 0.05\pi$, compared to the 20 Trotter steps shown in Sec. III; our accuracy is higher when restricted to only 20 Trotter steps.

Next, we plot the same for a wide range of bond dimensions to investigate the convergence of the rescaled data (see Fig. S5 of Supplemental Material [19] for intermediate temperatures on the 6×6 grid). We find that

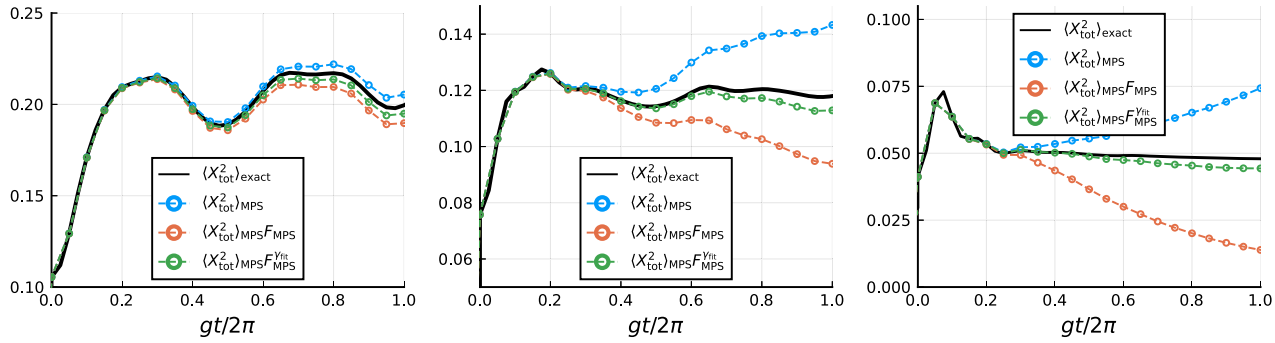


FIG. 12. Comparison of scaled and unscaled $\langle \boldsymbol{X}^{\mathbf{2}}_{\rm tot}\rangle$ to exact data for different temperatures. For all temperatures, curves scaled by a fractional power of fidelity agree much better with the exact data than either unscaled curves or curves scaled by fidelity. Here, the system is on a 6×6 grid, and the MPS data are computed with $\chi = 4096$. The states from left to right use the low-, intermediate-, and high-energy state preparations, respectively, as described in Sec. VA, and γ is extracted from the fits reported in Fig. S4 of Supplemental Material [19].

convergence to the exact data is greatly accelerated by rescaling compared to the unrescaled data. In both cases, the error tends to increase with the evolution time.

To characterize the error of the rescaled data, we plot the maximum error between the rescaled and exact data over the time range $0 \le gt/2\pi \le 1$ for all system sizes and bond dimensions for which we have exact data. As for the TFIM, the scaling of the error ϵ is well described by a linear relation between $\log\epsilon$ and the scaled bond dimension $\log_2 \chi/n$. These fits are consistent with the behavior observed for the 6×6 grid data across a range of bond dimensions (see Fig. S7 of Supplemental Material [19]), giving us confidence that the error predictions will also apply to larger sizes. We note that while the exact data lie slightly outside the plotted intervals in some cases, this is expected because the error interval plots the typical value

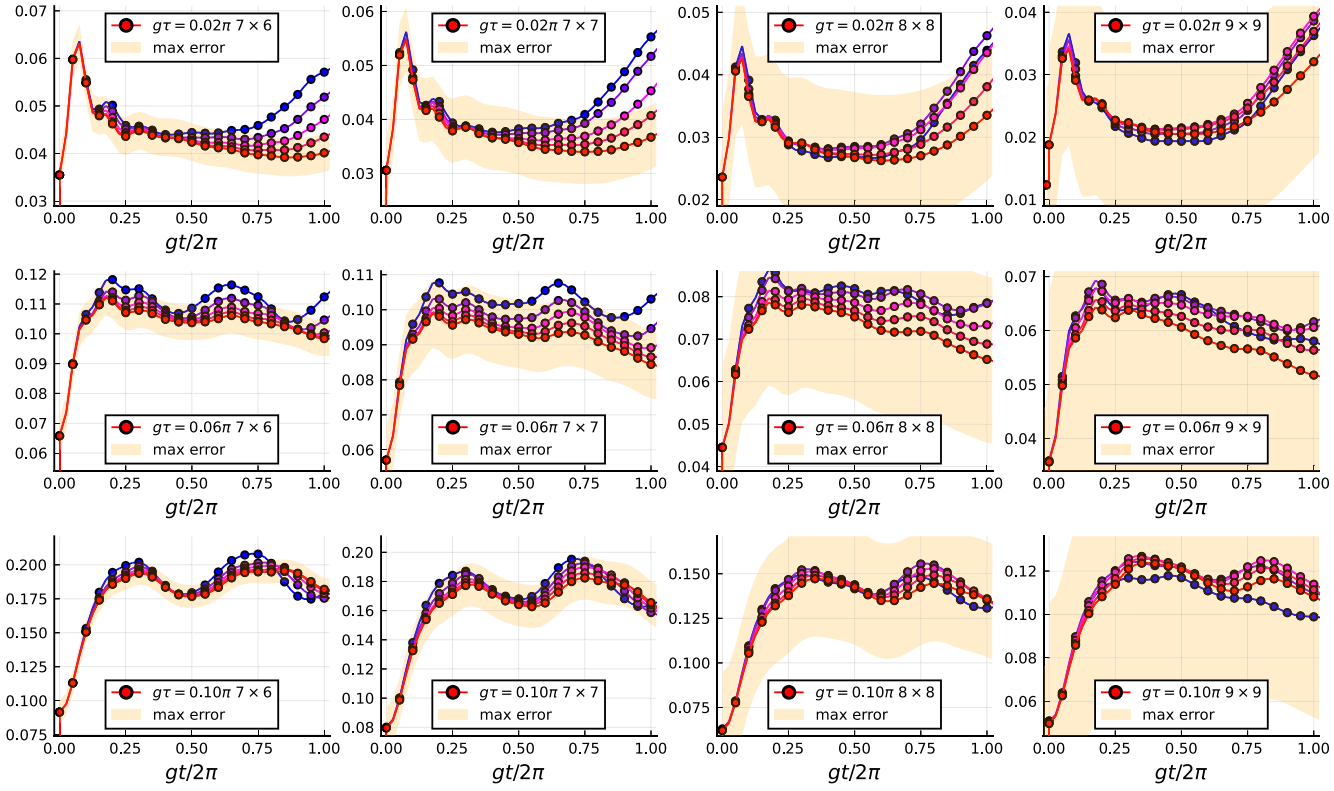


FIG. 13. Numerical results for the XY order parameter dynamics on larger grids. The plots show the rescaled $\langle X^2_{\rm tot}\rangle_{\gamma_{\rm fit}}$ for different grid sizes, with the maximum bond dimension ranging from 128 (blue) to 2048 (red). The shaded areas correspond to the extrapolated maximum absolute error for a bond dimension of 2048, as determined from the fits reported in Fig. S6 of Supplemental Material [19].

of the error (maximized over the time window; see Fig. S6 of Supplemental Material [19]) rather than an upper bound.

Finally, we use our rescaling and error fits to extrapolate predictions beyond the reach of exact numerics. The results are shown in Fig. 13. Since the error estimate predicts a maximum error over the full time window, whereas actual errors are typically much smaller at early times, the convergence of the rescaled MPS is expected to be better than predicted for early times. As the extrapolation is extended to larger sizes, our error estimates become large compared to the physical signal.

VI. CONCLUSIONS

In this paper, we propose a heuristic approach to accelerate the convergence of MPS simulations, applied to the two-dimensional quantum spin systems. We observe that a smaller bond dimension than previously expected may be sufficient to simulate physical observables. This is because, for some observables, a low bond dimension estimate is already correlated with the exact value, differing from it to a good approximation only by a rescaling factor. More specifically, in the case of the transverse field Ising model the magnetization $\langle Z_{\mathrm{tot}}\rangle$ can be estimated by rescaling a low bond dimension MPS estimate $\langle Z_{\mathrm{tot}}\rangle_{\mathrm{MPS}}$ by the fidelity of MPS F_{MPS}. In the case of the correlation function of the Ising order parameter $\langle Z_{\mathrm{tot}}^2\rangle$, rescaling by F_{MPS} alone is insufficient. However, we empirically observe that using a scaling factor of the form $F_{\mathrm{MPS}}^{\gamma(n,\chi)}$ is sufficient to accelerate the convergence of $\langle Z_{\mathrm{tot}}^2\rangle$ from numerical MPS simulations. The parameter $\gamma(n,\chi)$ is extrapolated from numerical simulations on grids up to 36 qubits and extended to larger grids. For sizes where exact numerical simulations are not available, it is instructive to compare our results to the available experimental data—specifically, the recently reported 7×8 TFIM. Not only were we able to accurately predict the converged results for $\langle Z_{\mathrm{tot}}^2\rangle$ prior to the release of Quantinuum's improved error mitigation [32], but the updated experimental results [18] also match our numerical results within the estimated error bounds, demonstrating the predictive power of our method. We also extended our simulations to larger TFIMs up to 11×11. However, our extrapolation is based on exact results for systems of limited size, and it might not be reliable for such large systems. We find that this behavior generalizes to other quantum spin systems. More specifically, we observe a similar accelerated convergence of MPS in simulations of the quench dynamics of the 2D XY model.

ACKNOWLEDGMENTS

We thank Sergio Boixo, Vadim Smelyanskiy, Michael Foss-Feig, and Andrew Potter for useful discussions and comments.

S. M. designed the rescaling heuristic, developed the TFIM MPS simulator, and ran the 2D and 3D TFIM simulations. B. W. developed the XY model MPS simulator and ran the 2D XY simulations. K. K. developed the theoretical analysis and interpretation. N. A. and T. W. designed the exact simulator and ran exact simulations for grids up to 6×7. S. I. designed an alternative exact simulator and ran exact simulations for grids up to 6×8. B. V. designed the tensor network simulator and ran exact simulations on 7×8 grids up to step 4. S. M., K. K., and B. W. performed the MPS analysis. All authors contributed to the writing of the paper.

DATA AVAILABILITY

The data supporting the findings of this study are available in Ref. [42].

[1] F. Arute, K. Arya, R. Babbush, D. Bacon, J. C. Bardin, R. Barends, R. Biswas, S. Boixo, F. G. Brandao, D. A. Buell *et al.*, *Quantum supremacy using a programmable superconducting processor*, Nature (London) **574**, 505 (2019).

[2] A. Morvan, B. Villalonga, X. Mi, S. Mandrà, A. Bengtsson, P. Klimov, Z. Chen, S. Hong, C. Erickson, I. Drozdov *et al.*, *Phase transitions in random circuit sampling*, Nature (London) **634**, 328 (2024).

[3] T. I. Andersen, N. Astrakhantsev, A. H. Karamlou, J. Berndtsson, J. Motruk, A. Szasz, J. A. Gross, A. Schuckert, T. Westerhout, Y. Zhang *et al.*, *Thermalization and criticality on an analogue–digital quantum simulator*, Nature (London) **638**, 79 (2025).

[4] A. Ransford, M. Allman, J. Arkinstall, J. Campora III, S. F. Cooper, R. D. Delaney, J. M. Dreiling, B. Estey, C. Figgatt, A. Hall *et al.*, *Helios: A 98-qubit trapped-ion quantum computer*, arXiv:2511.05465.

[5] D. Gao, D. Fan, C. Zha, J. Bei, G. Cai, J. Cai, S. Cao, F. Chen, J. Chen, K. Chen *et al.*, *Establishing a new benchmark in quantum computational advantage with 105-qubit Zuchongzhi 3.0 processor*, Phys. Rev. Lett. **134**, 090601 (2025).

[6] H.-L. Liu, H. Su, S.-Q. Gong, Y.-C. Gu, H.-Y. Tang, M.-H. Jia, Q. Wei, Y. Song, D. Wang, M. Zheng *et al.*, *Robust quantum computational advantage with programmable 3050-photon Gaussian boson sampling*, arXiv:2508.09092.

[7] R. Babbush, R. King, S. Boixo, W. Huggins, T. Khattar, G. H. Low, J. R. McClean, T. O'Brien, and N. C. Rubin, *The grand challenge of quantum applications*, PRX Quantum **7**, 020101 (2025).

[8] J. M. Deutsch, *Quantum statistical mechanics in a closed system*, Phys. Rev. A **43**, 2046 (1991).

[9] M. Srednicki, *Chaos and quantum thermalization*, Phys. Rev. E **50**, 888 (1994).

[10] J. M. Deutsch, *Eigenstate thermalization hypothesis*, Rep. Prog. Phys. **81**, 082001 (2018).

[11] A. Bakshi, A. Liu, A. Moitra, and E. Tang, *High-temperature Gibbs states are unentangled and efficiently preparable*, in *2024 IEEE 65th Annual Symposium on*

Foundations of Computer Science (FOCS) (2024), pp. 1027–1036.
[12] E. Leviatan, F. Pollmann, J. H. Bardarson, D. A. Huse, and E. Altman, *Quantum thermalization dynamics with matrix-product states*, arXiv:1702.08894.
[13] T. Rakovszky, C. W. von Keyserlingk, and F. Pollmann, *Dissipation-assisted operator evolution method for capturing hydrodynamic transport*, Phys. Rev. B **105**, 075131 (2022).
[14] X. Mi, P. Roushan, C. Quintana, S. Mandra, J. Marshall, C. Neill, F. Arute, K. Arya, J. Atalaya, R. Babbush *et al.*, *Information scrambling in quantum circuits*, Science **374**, 1479 (2021).
[15] D. A. Abanin, R. Acharya, L. Aghababaie-Beni, G. Aigeldinger, A. Ajoy, R. Alcaraz, I. Aleiner, T. I. Andersen, M. Ansmann, F. Arute *et al.*, *Observation of constructive interference at the edge of quantum ergodicity*, Nature (London) **646**, 825 (2025).
[16] T. Begušić and G. K.-L. Chan, *Real-time operator evolution in two and three dimensions via sparse Pauli dynamics*, PRX Quantum **6**, 020302 (2025).
[17] G. Park, J. Gray, and G. K.-L. Chan, *Simulating quantum dynamics in two-dimensional lattices with tensor network influence functional belief propagation*, arXiv:2504.07344.
[18] R. Haghshenas *et al.*, *Digital quantum magnetism on a trapped-ion quantum computer*, Nature (London) **653**, 56 (2026).
[19] See Supplemental Material at http://link.aps.org/supplemental/10.1103/qq2m-v44w for details on MPS ordering, 3D TFIM simulations, and additional scaling results, which includes Ref. [18].
[20] L. Onsager, *Crystal statistics. I. A two-dimensional model with an order-disorder transition*, Phys. Rev. **65**, 117 (1944).
[21] P. Pfeuty, *The one-dimensional Ising model with a transverse field*, Ann. Phys. (N.Y.) **57**, 79 (1970).
[22] S. Sachdev, *Quantum phase transitions*, Phys. World **12**, 33 (1999).
[23] M. Schmitt, M. M. Rams, J. Dziarmaga, M. Heyl, and W. H. Zurek, *Quantum phase transition dynamics in the two-dimensional transverse-field Ising model*, Sci. Adv. **8**, eabl6850 (2022).
[24] T. Kuwahara, T. Mori, and K. Saito, *Floquet–magnus theory and generic transient dynamics in periodically driven many-body quantum systems*, Ann. Phys. (Amsterdam) **367**, 96 (2016).
[25] D. A. Abanin, W. De Roeck, W. W. Ho, and Fçois Huveneers, *Effective Hamiltonians, prethermalization, and slow energy absorption in periodically driven many-body systems*, Phys. Rev. B **95**, 014112 (2017).
[26] M. Heyl, P. Hauke, and P. Zoller, *Quantum localization bounds Trotter errors in digital quantum simulation*, Sci. Adv. **5**, eaau8342 (2019).
[27] W. W. Ho, T. Mori, D. A. Abanin, and E. G. Dalla Torre, *Quantum and classical Floquet prethermalization*, Ann Phys. (Amsterdam) **454**, 169297 (2023).
[28] Y. Zhou, E. M. Stoudenmire, and X. Waintal, *What limits the simulation of quantum computers?*, Phys. Rev. X **10**, 041038 (2020).
[29] K. H. Marti and M. Reiher, *DMRG control using an automated Richardson-type error protocol*, Mol. Phys. **108**, 501 (2010).
[30] R. Mondaini, K. R. Fratus, M. Srednicki, and M. Rigol, *Eigenstate thermalization in the two-dimensional transverse field Ising model*, Phys. Rev. E **93**, 032104 (2016).
[31] R. Mondaini and M. Rigol, *Eigenstate thermalization in the two-dimensional transverse field Ising model. II. Off-diagonal matrix elements of observables*, Phys. Rev. E **96**, 012157 (2017).
[32] R. Haghshenas, E. Chertkov, M. Mills, W. Kadow, S.-H. Lin, Y.-H. Chen, C. Cade, I. Niesen, T. Begušić, M. S. Rudolph *et al.*, *Digital quantum magnetism at the frontier of classical simulations*, arXiv:2503.20870.
[33] V. L. Berezinski, *Destruction of long-range order in one-dimensional and two- dimensional systems possessing a continuous symmetry group. II. Quantum systems*, Sov. Phys. JETP **34**, 610 (1972).
[34] J. M. Kosterlitz and D. J. Thouless, *Long range order and metastability in two dimensional solids and superfluids. (Application of dislocation theory)*, J. Phys. C **5**, L124 (1972).
[35] J. M. Kosterlitz and D. J. Thouless, *Ordering, metastability and phase transitions in two- dimensional systems*, J. Phys. C **6**, 1181 (1973).
[36] E. Loh, D. J. Scalapino, and P. M. Grant, *Monte Carlo studies of the quantum XY model in two dimensions*, Phys. Rev. B **31**, 4712 (1985).
[37] H. Q. Ding and M. S. Makivic, *Kosterlitz-Thouless transition in the two-dimensional quantum XY model*, Phys. Rev. B **42**, 6827 (1990).
[38] H.-Q. Ding, *Phase transition and thermodynamics of quantum XY model in two dimensions*, Phys. Rev. B **45**, 230 (1992).
[39] S. Zhang and K. J. Runge, *Green's-function Monte Carlo study of the two-dimensional, spin-1/2 XY ferromagnet*, Phys. Rev. B **45**, 1052 (1992).
[40] P. Olsson, *Monte Carlo analysis of the two-dimensional XY model. II. Comparison with the Kosterlitz renormalization-group equations*, Phys. Rev. B **52**, 4526 (1995).
[41] Gé Vidal, *Efficient simulation of one-dimensional quantum many-body systems*, Phys. Rev. Lett. **93**, 040502 (2004).
[42] S. Mandrà, B. Ware, N. Astrakhantsev, S. Isakov, B. Villalonga, T. Westerhout, and K. Kechedzhi, *Data for "A heuristic for matrix product state simulation of out-of-equilibrium dynamics of two-dimensional quantum spin systems"*, Zenodo, 10.5281/zenodo.21829368 (2026).